Lawrence Berkeley National Laboratory

Title
Experimental and numerical investigation into rapid cooling of rock salt related to high frequency cycling of storage caverns

Permalink

Authors
Blanco-Martín, Laura
Rouabhi, Ahmed
Billiotte, Joël
et al.

Publication Date
2018-02-01

DOI

Peer reviewed

Experimental and numerical investigation into rapid cooling of rock salt related to high frequency cycling of storage caverns

Laura Blanco-Martín[a] Ahmed Rouabhi[a] Joël Billiotte[a] Faouzi Hadj-Hassen[a] Bruno Tessier[a] Grégoire Hévin[b] Cyrille Balland[c] Emmanuel Hertz[d]

Abstract

High frequency cycling of salt caverns is becoming common practice to meet the needs of energy markets and to foster underground energy storage. In the case of rapid cooling, tensile stresses and thermally-induced fractures can appear in the surrounding rock, with potential detrimental consequences to the integrity of the storage project. To further investigate the effects of rapid cycles on the integrity of rock salt, a thermo-mechanical test was performed in a salt mine. It consisted in cooling rapidly several times a salt surface of 10 m² ($\Delta T = -20$ °C in about 8 h). Extensive monitoring allowed tracking the thermo-mechanical response of the rock, including possible fracture creation and propagation. Although more research is needed, the test demonstrated that tensile fracturing due to rapid cooling is possible. Thermo-mechanical modeling allowed reproducing fairly well the location, orientation and timing of the first fracture; indeed, fractures should be avoided to ensure cavern integrity, and therefore knowledge about the critical zones where fractures could appear is sufficient at the design stage.

Keywords: Field test, Temperature drop, Tensile stresses, Salt caverns, High frequency cycling, Thermo-mechanical modeling

1. Introduction

Leached salt caverns have been used since the late 1940s to store (or dispose of) fluids underground.[1, 2, 3, 4] The main factors leading to this success are the very low porosity and near-zero permeability of undisturbed rock salt.[5, 6, 7] In addition, the deliverability rate of salt caverns is much higher than that of depleted reservoirs or aquifers.[8] Among the stored fluids, hydrocarbons (oil, natural gas) have dominated in the storage facilities worldwide. Apart from strategic storage, these fluids are typically injected when the demand is low (summer) and withdrawn when the demand is high (winter); in such scenario, caverns undergo yearly cycles during which the stress state and temperature change at the cavern wall and the surrounding rock. The mechanical stability and hydraulic tightness of salt caverns for hydrocarbon storage have been widely investigated (see for instance[5, 9, 10, 11, 12, 13, 14]). Since temperature changes are small for low injection/withdrawal rates, thermal effects do not propagate far from the cavern wall and are often neglected.[15]

In the recent years, the liberalization of energy markets and the use of the underground to foster renewable energy penetration in the energy matrix have brought about new scenarios in which new fluids and operating conditions are encountered. Specifically, compressed air energy

storage(CAES) in salt caverns is raising attention,[16] and a move towards high-frequency cycles (i.e., weeks, days or even less) has been observed for natural gas and hydrogen.[17, 18] These operating conditions need to be thoroughly investigated because in the case of a rapid depressurization, the gas cools down quickly and heat transfer with the surrounding host rock is limited. Thermal contraction of the rock occurs, which can lead to the onset of tensile stresses. Since the tensile strength of rock salt is quite small (1–2 MPa), tensile stresses must be managed (better avoided) to preserve the barrier integrity of the salt rock mass. Some numerical studies suggest that tensile stresses induced by rapid cooling are transient by nature, and also that the depth of penetration of possible thermally-induced fractures is small; consequently, cavern integrity is unlikely to be threatened.[17, 19, 20, 21, 22, 23] Since salt caverns are not accessible, experimental evidence that could support or contradict the numerical predictions is limited,[24, 25] and as a result a sound conclusion has not yet been reached. In order to gain more insight, the Solution Mining Research Institute (SMRI) has launched a research program to further investigate the effects of high frequency cycling on the integrity of rock salt.

In the context of the SMRI research program, a thermo-mechanical test was performed in a salt mine in North-Eastern France. This unique test consisted of three cooling-warming cycles followed by two cooling stages applied to a salt surface of 10 m^2. The cooling was applied rapidly (ΔT=−20°C in about 8 h), and monitoring of the test was extensive to allow investigating the thermo-mechanical response of the rock, including possible fracture creation and propagation. In this paper, we first describe the field test and its principal outcomes. Then, we present results of thermo-mechanical modeling performed after the test to help interpret the experimental data and to evaluate the capabilities of the numerical tools commonly used in cavern design to reproduce the test results, and in particular, the location, orientation and timing of the first fracture. A continuum approach is used, since fractures should be avoided to ensure cavern integrity, and knowledge about the critical zones where fractures could appear is sufficient at the design stage. As it will be shown, the agreement between measurements and simulation results is quite satisfactory. Overall, even if more research is necessary, this experiment has demonstrated that rapid cooling of rock salt can lead to thermally-induced fracturing. In this sense, current design criteria and operational conditions of salt storage caverns should be adapted to minimize the effects of rapid depressurizations.

2. Field test at the Varangéville mine

A salt slab was selected to investigate the impacts of rapid cooling on the thermo-mechanical behaviour of rock salt. The test was performed in the Varangéville salt mine (North-Eastern France). This mine is operated by the room and pillar method and is located at the base of the third layer of the Keuper salt formation, where the global salt content is around 94%. The salt layer sits above a marl layer and underneath a sandstone-marl layer. For

the purposes of the experiment, a dead-end gallery (niche) was excavated at a depth of about 120 m, with dimensions 17.5×12×4.5 m³(length, width, height). To perform the test, a 13×12×1.3 m³ slab was left unexcavated at the floor of the niche. The distance from the top surface of the salt block to the salt-marl contact is about 1.5 m.

In order to isolate the effects of rapid cooling on the stress state, the influence of the in situ stress field was minimized. For this purpose, two vertical slots were cut parallel to the niche axis, at a distance of 1.1 m and 0.7 m from the West and East walls, respectively. The slots were 0.1 m wide and 1.5 m high, and were backfilled prior to the test to prevent heat convection. Thanks to the slots, the salt block is free at four surfaces: top, front and two sides. Fig. 1a shows a plan view of the experimental niche.
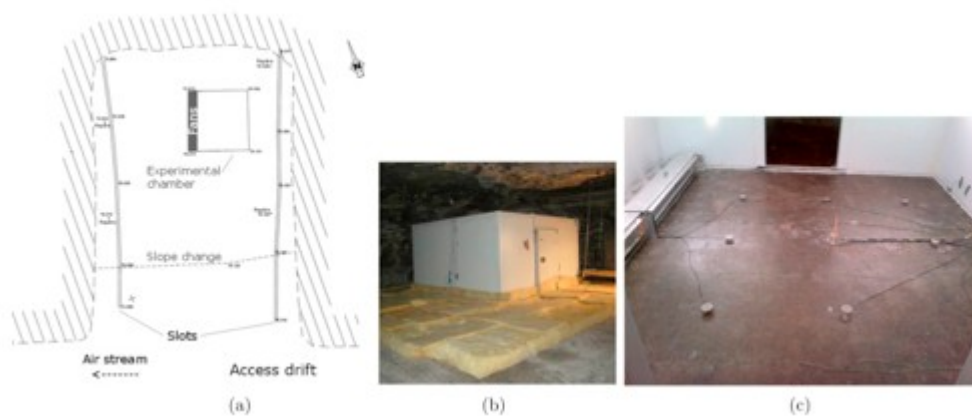

Fig. 1. (a) Plan view of the experimental niche, including location of the experimental chamber and the two slots; (b) View of the experimental chamber surrounded by the insulation cover (the height of the chamber is 2.23 m and the width of the walls [HD polyurethane] is 10 cm); (c) Inside view of the chamber (floor fans are visible in the left-hand side, as well as acoustic emission devices on the floor).

After excavation, the block was analyzed to identify possible cracks caused by the niche excavation or related to the salt structure (desiccation cracks, etc). Based on this analysis, it was decided to conduct the experiment in the rear part of the slab, close to the niche end. A square surface of 10 m² was conditioned on top of the salt block to perform the test. The experimental surface can be seen in Fig. 1a. On this surface, an experimental chamber was built; it allowed cooling the salt surface and the underlying salt rock mass. Fig. 1b shows an outside view of the chamber and Fig. 1c shows a view of the inside with some equipment (details will be given below). The chamber was designed so that a temperature drop of 40 °C could be applied to the salt surface (from the ambient temperature to about −25 °C). The cooling device consists of a 7.5 kW refrigeration unit that cools down the air inside the chamber. In order to keep the niche temperature as constant as possible, the compressor was placed in the access gallery, next to the niche entrance. The mine is ventilated, and temperature is about constant in the drifts (14.5 °C approximately at a depth of 120 m, corresponding to the geothermal gradient).

To ensure a uniform cold production inside the chamber, the cold air was blown through an evaporating system placed in the ceiling along the right (East) wall of the room. To reduce heat losses below the walls and through the rock mass outside the chamber, a 20 cm thick rockwool insulation cover was placed on the salt floor around the chamber during the cooling stages. The insulation cover is displayed in Fig. 1b. The optimal distance from the chamber that should be insulated was estimated numerically to be about 2.5 m.[26] This way, the energy required to cool down the salt surface is reduced by 30%, yielding 150 W/m^2.

In order to enhance the convective flux inside the chamber (and therefore, the transfer of thermal energy with the rock), eight fans were placed on the floor next to the left wall (nominal range of 9.5 m/s); they can be seen in Fig. 1c. The air speed is thereby increased, which increases the heat transfer coefficient between the air and the salt surface.

During the experiment, three cooling-warming cycles were performed, followed by two additional cooling phases. For each of the cycles, the cold air flow was applied for 28 days and the average temperature of the salt surface decreased to about −6 °C. Then, the air flow was stopped for at least six weeks so that temperature inside the chamber and in the salt block could equilibrate with the mine temperature (to facilitate warming, the insulation cover was removed during the warming periods). The last two stages consisted in cooling the salt surface down to temperatures of −6 °C and −25 °C for a time period of 14 and 21 days, respectively. They were conducted to investigate the effects of a further decrease in temperature on the stress state and on the onset and propagation of possible cracks. Fig. 2 displays the loading history (measured air temperature in the chamber over time). As the figure shows, during each cycle the air temperature reached −8.5 °C (−27 °C for the last stage) in a very short time (about 8 h). Likewise, the temperature rise was very fast during the warming phases, although about three times slower than the cooling rate. At the end of the first four cooling stages, the air temperature reached −9 °C (−27.6 °C for the fifth stage).
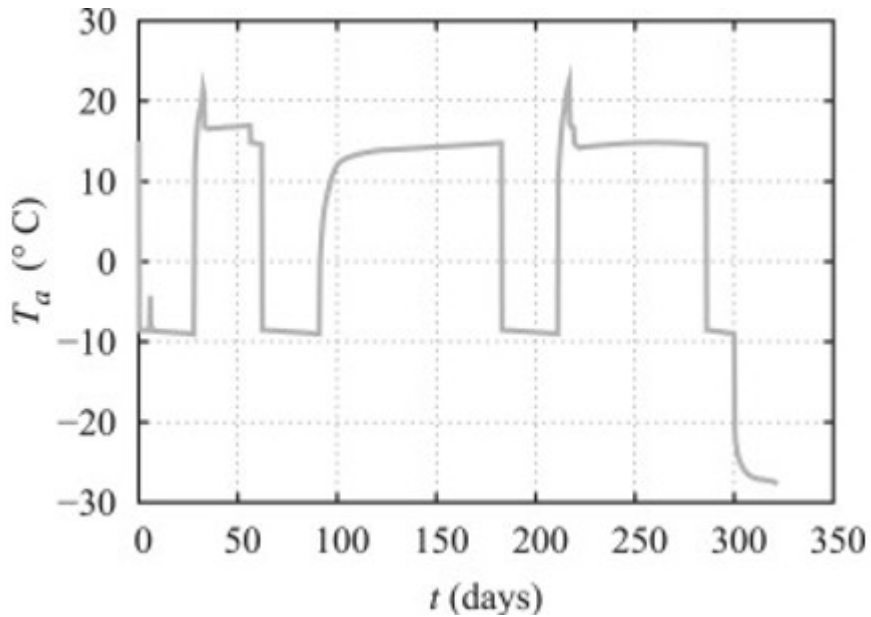
Fig. 2. Air temperature inside the chamber. The maximum value of 21 °C recorded during cycles 1 and 3 is due to the use of an electric heater during the first week of warming.

An extensive measurement program was defined to get as much insight as possible.[26] Temperature sensors (Pt100 and thermocouples) were installed at different locations inside the chamber and outside the chamber below the insulation cover. Inside the chamber, they were placed at the salt surface, at 1 cm depth and in a vertical borehole drilled at the center of the room, allowing to sample temperature as deep as 80 cm. Outside the chamber, the sensors were placed at a depth of 1 cm. The heat fluxbetween the air and the salt surface was also measured, using a flux sensor placed on the floor, in the central part of the chamber. Strain gauges were placed on the salt surface and in the central borehole. An ultrasonic network was also set up, comprising 5 emitters and 12 receivers (see Fig. 1c). To get three-dimensional gridding, the receivers were placed on the salt surface and underneath; for this purpose, 4 inclined boreholes were drilled from outside the chamber to a depth of 60 cm below the test surface. An imaging system was also set up; it allowed tracking the formation and propagation of possible fractures. Four digital cameras (resolution of 3 px/mm) attached to the ceiling of the room covered the entire floor of the chamber. A rotating infrared camera was also placed at the ceiling to track the room surface temperature. All these techniques allowed a full characterization of possible fractures: time of creation, location and orientation, size, number, etc.

During the first cycle, a macro-fracture was visible after about six hours of cooling. It was located perpendicular to the air flow, about one meter from the fans (area with coldest temperature), and extended rapidly over more than one meter. At the end of the first cycle, the crack aperture was less than 1 mm (measured with dial gauges). In addition to this macro-crack, many micro-cracks (imperceptible to the naked eye) were present over the entire surface at that time. They were closed and shallow in appearance. In

subsequent cycles, pre-existing fractures reopened and spread. Additionally, new cracks were created. Therefore, a fracture networkdeveloped progressively during the cycles; however, it should be noted that the extension of the cracks decreased with the number of cycles. Measurements from acoustic emission are consistent with the images interpretation[27]: the number of events reduced from one cycle to the next, with the first cycle producing 2–3 more events than the rest. Fig. 3 shows the visible fractures developed throughout the experiment. It can be seen how these fractures tend to join over time. At the end of the test, the maximum crack width was 1–1.2 mm. The analysis of the last cooling stage shows that a further temperature decrease increases the width of crack opening and enhances the creation of new fractures.
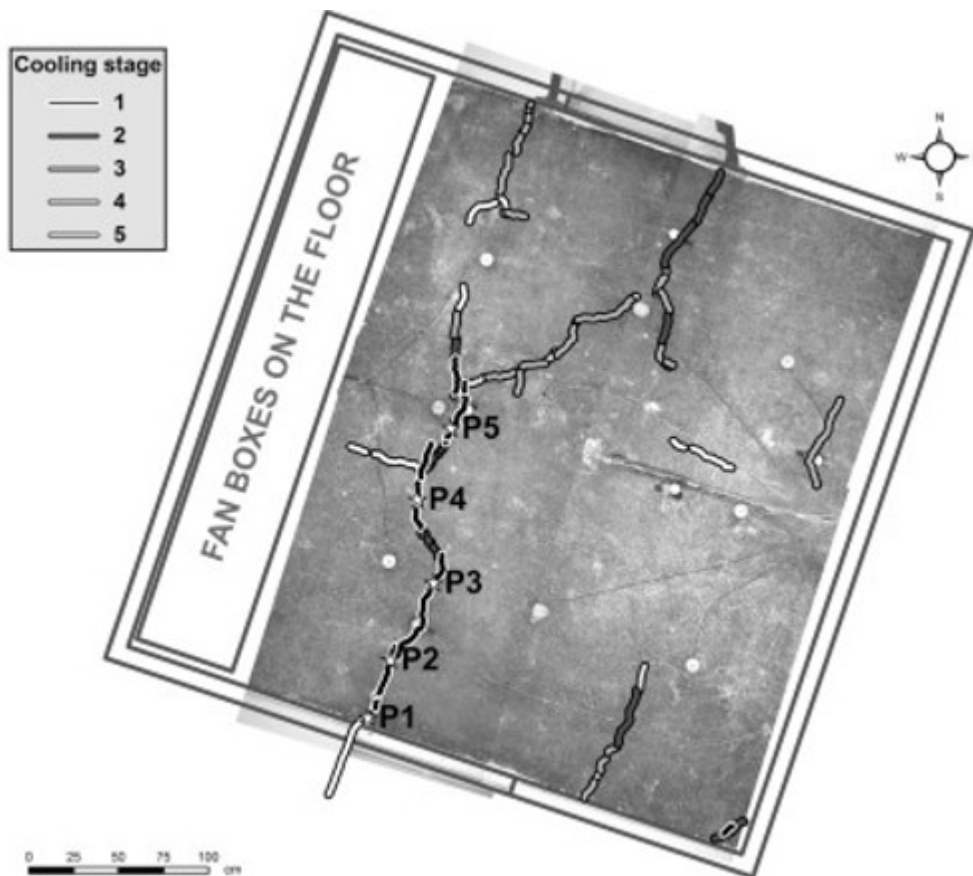

Fig. 3. Visible fractures developed during the different cooling stages of the experiment.

After the test, four cores were drilled to a depth of 2 m. Fig. 4 displays a view of the core drilled on the main crack, between points P3 and P4 in Fig. 3; this crack is visible down to a depth of 75–80 cm, where it leaves the core, but a potential axial closed crack can be observed until a depth of 1.25 m.
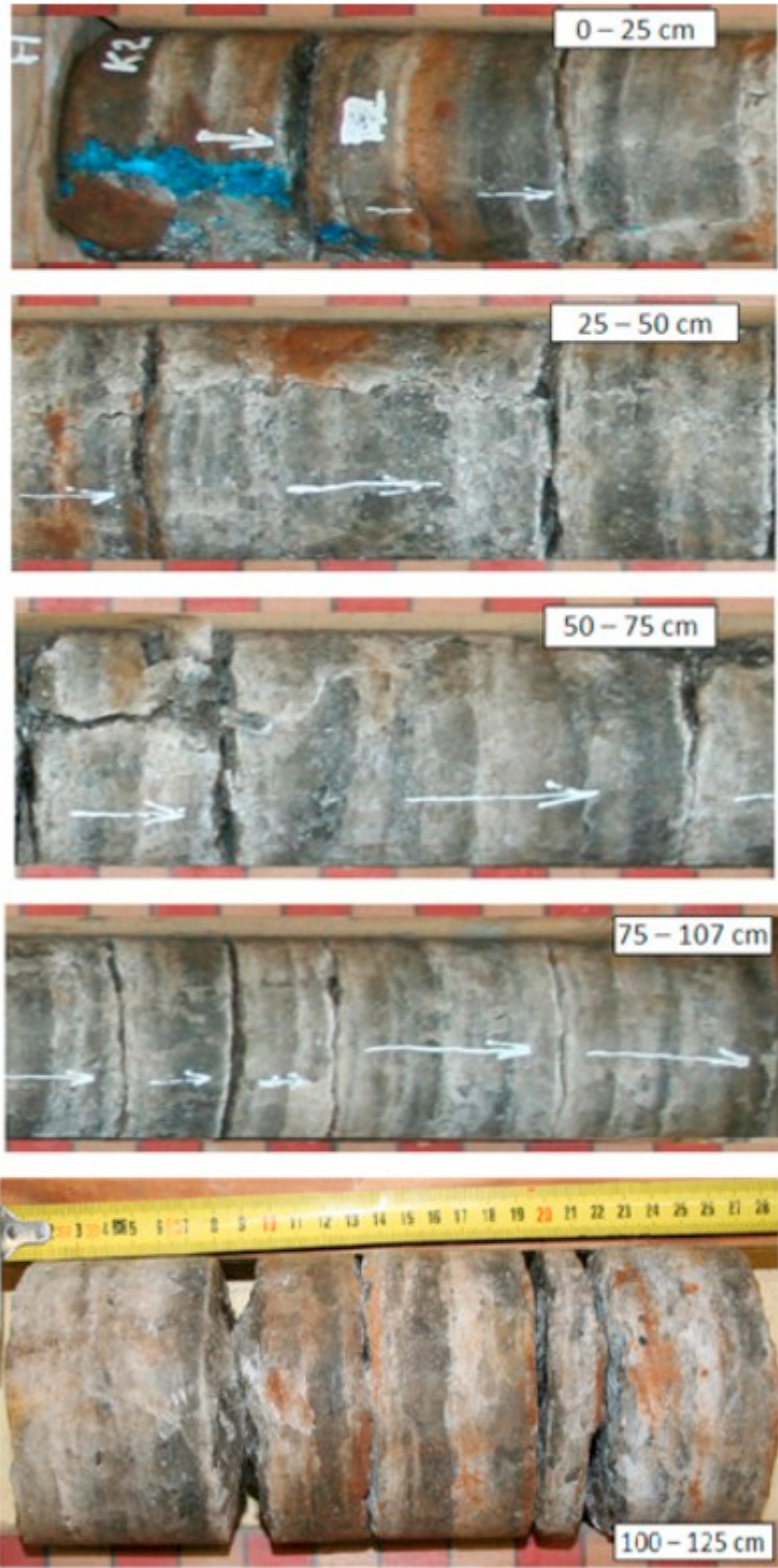
Fig. 4. View of core K2, drilled on the main fracture observed (core diameter is 90 mm).

3. Thermo-mechanical modeling

3.1. Introduction

Modeling was performed after the test to (i)help interpret experimental results, and (ii)evaluate the capabilities of the numerical tools commonly used in cavern design to reproduce the experimental data, and in particular, the location, orientation and timing of the first fracture. Indeed, to ensure cavern integrity fractures should be avoided, so we focus on the conditions under which fractures could appear (rather than fracture propagation), for which a continuum modeling approach is justified. In those cases in which fracture propagation is important, a continuum modeling approach should be coupled with a numerical method that allows fracture evolution, such as the extendend finite element method (XFEM).[28]

Proper modeling of the experiment requires coupling between different processes, particularly thermal and mechanical. Indeed, hydraulic processes are less important in the current case due to two main reasons. First, the intercrystalline space of rock salt, although very small (porosity values in the order of 0.1% are not unusual), is not filled with water, but with saturated brine, whose freezing point is about -21 °C. Second, due to the low porosity of rock salt, the thermal expansivities of the porous medium and of the grains are very similar, and therefore differential effects, which could induce pore pressure changes in low permeability materials,[29]can be neglected. The governing field equations of the thermo-mechanical problem are the balance laws of momentum and thermal energy, which read respectively

$$(1) \quad \nabla \cdot \underline{\underline{\sigma}} + \rho \vec{g} = 0 \qquad \rho C_p \dot{T} + \nabla \cdot \vec{\psi} = 0$$

where $\underline{\underline{\sigma}}$ is the Cauchy stress tensor, $\vec{g}$ is the gravity acceleration vector, ρ is mass density, C_p is the heat capacity, $\dot{T}$ is the material derivative of the temperature T, $\vec{\psi}$ is the heat flux vector and $\nabla \cdot$ is the divergence operator. Eq. (1) needs to be completed with boundary conditions, initial conditions and constitutive laws for $\underline{\underline{\sigma}}$ and $\vec{\psi}$. As for the heat flux, Fourier's law of heat conduction, $\vec{\psi} = -\lambda \vec{\nabla} T$, where λ is the thermal conductivityof the material, is used. Regarding the stress tensor, we use a constitutive law based on the additive decomposition of the strain tensor into elastic, thermal and viscoplastic components. Under the assumption of isotropic material behaviour, infinitesimal strains and negative sign for compressive stress and strain, this yields

$$(2) \quad \underline{\underline{\varepsilon}} = \frac{1+\nu}{E}(\underline{\underline{\sigma}} - \underline{\underline{\sigma}}_0) - \frac{\nu}{E}\text{tr}(\underline{\underline{\sigma}} - \underline{\underline{\sigma}}_0)\underline{\underline{1}} + \alpha_{th}(T - T_0)\underline{\underline{1}} + \underline{\underline{\varepsilon}}_{vp}$$

where ν is the Poisson's ratio, E is the Young's modulus, α_{th} is the linear thermal expansion coefficient, T_0 is the initial temperature, tr() is the trace operator, $\underline{\underline{\sigma}}_0$ is the initial stress tensor, $\underline{\underline{1}}$ is the identity tensor, and $\underline{\underline{\varepsilon}}_{vp}$ is the viscoplastic strain tensor, which describes the time-dependent behaviour of rock salt. In this study, the evolution law of $\underline{\underline{\varepsilon}}_{vp}$ is modeled using Lemaitre creep law,[30] which can be expressed

$$(3) \quad \underline{\underline{\dot{\varepsilon}}}_{vp} = \frac{3}{2}\dot{\gamma} q \underline{\underline{\sigma}}'$$

where $\underline{\sigma}'=\underline{\sigma}-\frac{1}{3}\mathrm{tr}(\underline{\sigma})\underline{1}$ is the deviatoric stress tensor, $q=3/2\|\underline{\sigma}'\|$ is the von Mises equivalent stress, and γ is an internal scalar variable whose evolution law accounts for material hardening and reads

$$(4)\quad d\gamma^{1/\alpha}dt=(qK(T))^{\beta/\alpha},\quad K(T)=K_r\exp(B(\tfrac{1}{T}-\tfrac{1}{T_r}))$$

where $(\alpha,\beta,K_r,B)\in\mathbb{R}^{+*4}$ are material constants and T_r is the absolute temperature at which B is determined.

As the above equations show, temperature affects the mechanical response through the coefficient of linear thermal expansion. Moreover, in the case of rock salt, temperature also affects the viscoplastic response. From mechanics to heat flow, the strength of the coupling is weaker, particularly if strains are small. Based on the strains measured during the test, we have performed one-way coupling from heat flow to geomechanics.

3.2. Model setup

In a first step, the temperature field is computed in space and time, and then thermo-mechanical modeling is performed. Both simulations model the same domain, displayed in Fig. 5. It extends 200 m along each axis, and it starts at the ground surface. Three horizontal layers are defined from the top: a 40 m thick sandstone-marl layer, a 80 m thick salt layer and a 80 m thick marl layer. The access drift and the experimental niche are at a depth of 119.8 m, 20 cm above the salt-marl contact. Note that in agreement with the experiment, the two slots created parallel to the niche axis reach the salt-marl contact in the model.
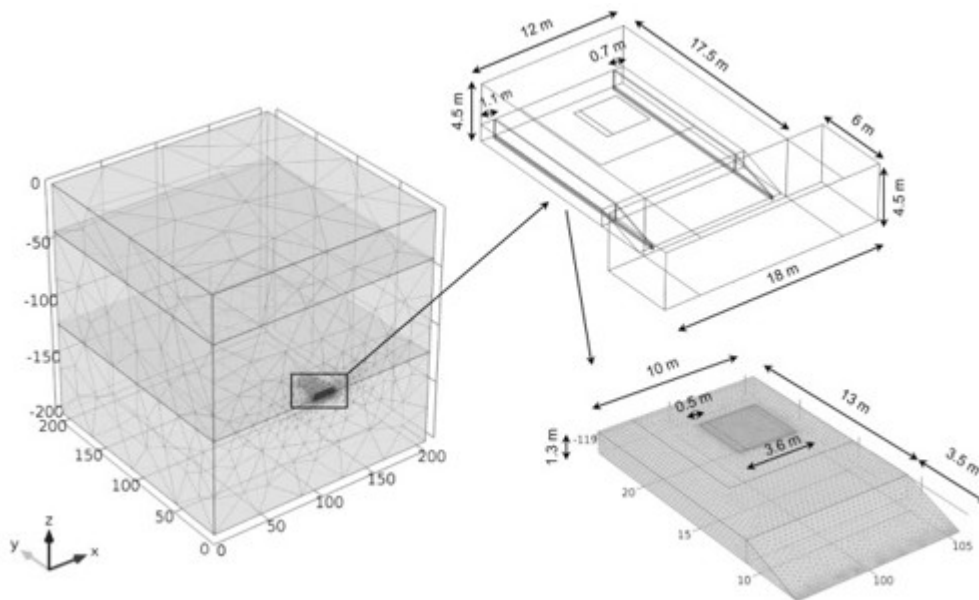

Fig. 5. View of the 3D model used in the simulations (left) and enlarged views of the niche (top right) and the salt block (bottom right). The domain is discretized into 202,990 tetrahedral elements, having minimum and maximum sizes of respectively 0.05 m (test zone) and 72 m (far from the niche).

In the thermal simulation, temperature is held constant at all outer planes ($x=0$, $x=200$ m, $y=0$, $y=200$ m, $z=-200$ m, $z=0$). It has been verified that

the thermal perturbation induced by the experiment does not reach these planes. The initial temperature is 14.5 °C in the whole domain (this simplification is justified due to the limited extent of the thermal perturbation as will be shown below), and the evolution of the air temperature, T_a, is given in Fig. 2. Heat transfer between the air and the salt surface is taken into account using Newton's law of cooling, defined as

$$(5) \quad \vec{\psi} \cdot \vec{n} = h(T - T_a)$$

where $\vec{n}$ is the outward-pointing unit normal vector and h is the heat transfer coefficient. The heat transfer coefficients have been determined inside and outside the chamber, during the cooling and the warming periods.[26] They are function of the air speed, independent of temperature, and their values have been confirmed by measurements of the heat flux and the temperature difference between the air and the salt surface. The regular value is $h=10$ W/m^2/K, but heat transfer is modified at some locations and periods. In particular, during cooling $h=22$ W/m^2/K below the fans, and $h=3.8x^2-21.96x+50.56$ W/m^2/K elsewhere in the chamber (x is a local coordinate system with origin at the chamber lower left corner, see Fig. 6). Below the insulation cover, $h=0.2$ W/m^2/K and in the backfilled slots, $h=2$ W/m^2/K.
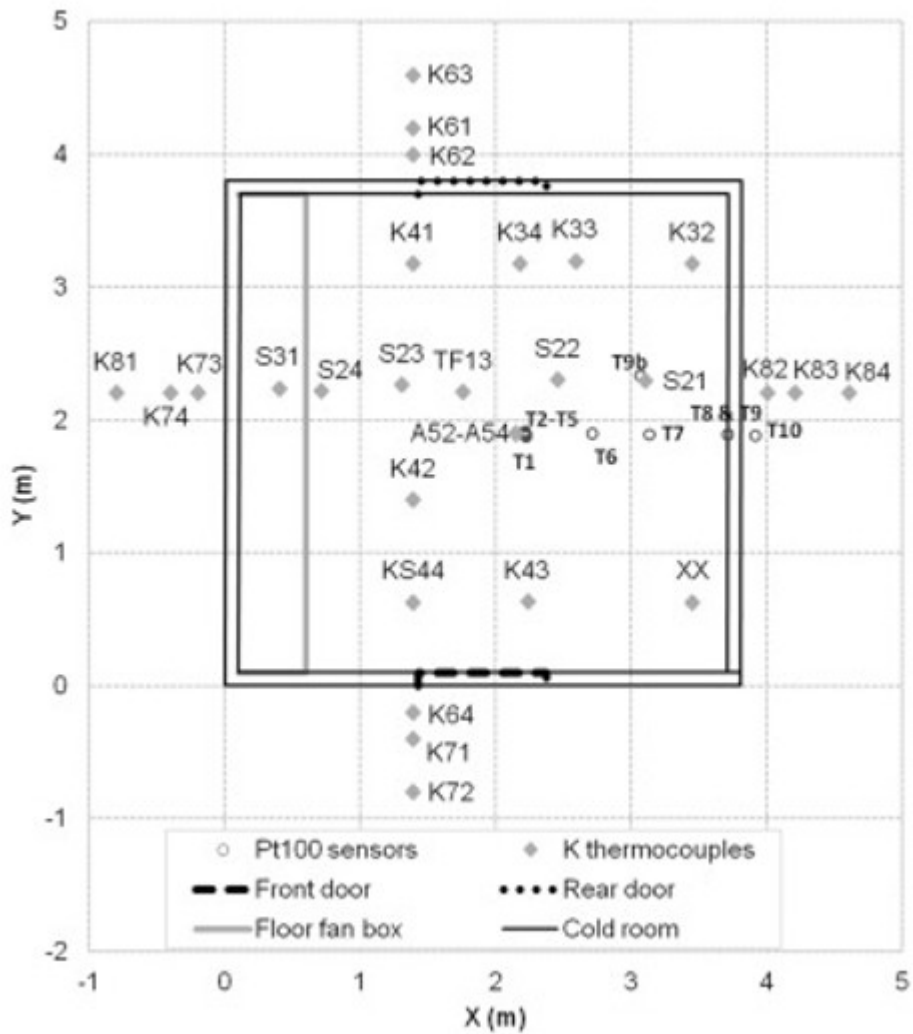
Fig. 6. Location of temperature sensors in a local reference system. Note that the thermocouples define two main orthogonal profiles, which extend outside the chamber. Air temperature is measured by sensors identified A52−A54. Pt100 sensors T2-T5 are placed at different depths in a vertical borehole. Sensor TF13 is a heat flux sensor.

As for geomechanics, the displacement normal to the vertical and bottom planes is blocked, and the $z=0$ plane is not constrained. Similarly to the thermal problem, it has been verified that the constrained boundaries are far enough and not affected by the processes induced by the experiment. The initial stress field is isotropic, equal to the lithostatic stress magnitude.

Table 1 lists thermo-mechanical properties of each layer. The marl and sandstone-marl layers are assumed to behave elastically. For the rock salt, the parameters of the Lemaitre model (Eq. (4)) have been obtained from creep tests performed at ambient temperature ($Tr=300.15$ K) by MINES ParisTech on salt samples from the Varangéville mine.

Table 1. Material constants of the rock layers included in the model.

Parameter (unit)	Sandstone-marl layer	Salt layer	Marl layer
Thermo-physical parameters			
ρ **(kg/m³)**	2500	2200	2300
Cp **(J/kg/K)**	850	850	900
λ **(W/m/K)**	2.5	6.8	2.9
Thermo-elastic parameters			
αth **(K−1)**	$1.5 \cdot 10{-}5$	$3 \cdot 10{-}5$	$1.5 \cdot 10{-}5$
E (GPa)	15	25	15
ν **(-)**	0.25	0.25	0.2
Viscoplastic parameters (unit system is MPa, K, days, µm/m)			
α	–	0.303	–
β	–	3.4	–
Kr	–	1.5	–
B	–	735.29	–

The thermal simulation covers the test duration, that in total was 322 days (three cycles and two subsequent cooling periods, see Fig. 2). This simulation is performed using the finite element (FEM) code COMSOL Multiphysics.[31] The geomechanical simulation, performed with the FEM code VIPLEF3D,[32, 33, 34] starts with the excavation of the drift, the niche and the two slots, assumed instantaneous and isothermal. This step is necessary to recalculate the stress field around the openings, and particularly in the salt block. Then, the elapsed time between the excavation and the beginning of the test is modeled (129 days), also in isothermal conditions. Finally, the test itself is modeled (thermo-mechanical coupling). The total modeled time in geomechanics is therefore 451 days.

3.3. Results

The temperature field computed over time compares well with experimental data. Fig. 6 shows the location of the temperature sensorsinside and outside the chamber, and Fig. 7 compares experimental and numerical temperatures

for some sensors. Note that after the first cooling stage, values of surface thermocouples appeared to be very noisy and it was decided to place them at a depth of 1 cm (except for sensor S31, which was located under the ventilation box). As it can be seen, the surface temperature inside the chamber is not uniform, but increases at further distances from the fans. Moreover, the length of the cooling phases allows temperature changes well below the salt surface and also beyond the chamber (this was actually a design requirement of the experiment). As Fig. 7 shows, negative temperatures are reached 80 cm below the salt surface in the second and subsequent cycles (sensor T5). Outside the chamber, the temperature of the salt surface is clearly affected by the experiment, and as expected the temperature gradient decreases at greater distances from the walls of the chamber.
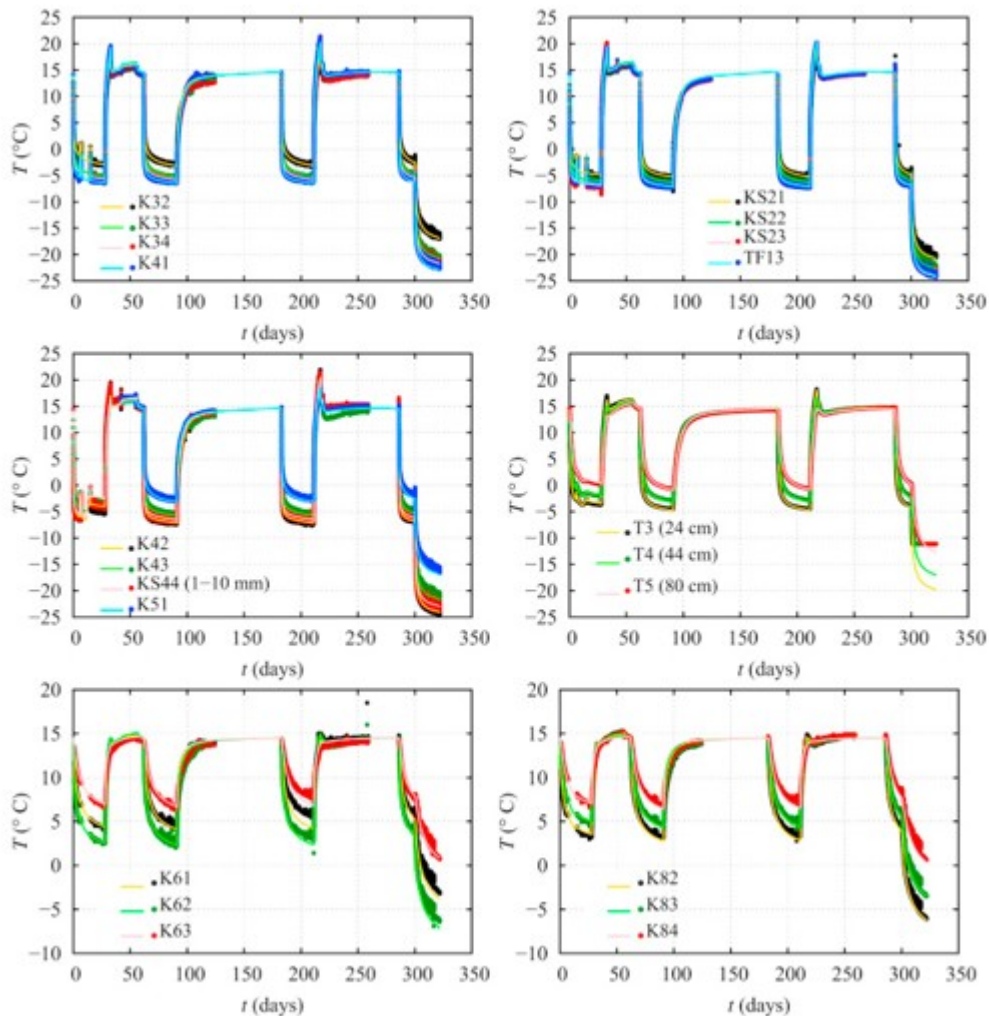

Fig. 7. Comparison between experimental data (symbols) and numerical results (lines) for temperature at several locations indicated in Fig. 6.

Overall, temperature measurements inside the chamber show similar distributions for the first four cooling periods, and more particularly for

periods 2–4. This suggests that the thermal loading on the rock salt was about the same during the cycles, and that the fractures created did not affect significantly the temperature field (note however that fracture aperture remained small, around 1–1.2 mm).

Regarding thermo-mechanical modeling, we first highlight that, owing to the use of a continuum modeling approach, the following analysis focuses on the first cycle, and particularly, the conditions that lead to the creation of the first fracture. Fig. 8 shows the maximum (i.e., least compressive) principal stress at the surface of the salt block ($z=-118.5$ m) after excavation. As it can be seen, the maximum principal stress is 2.76 MPa. This value is reached in the two small blocks left at both sides of the experimental block after cutting the slots, and is due to local effects induced by the free surfaces (some damage was observed in these zones before the test). On the surface of the experimental block, the stresses do no not exceed the tensile strength of the rock salt, assumed to be 1.5 MPa. The maximum principal stress at $t=129$ d (i.e., before the beginning of the test) is shown in Fig. 9. The comparison between Fig. 8, Fig. 9 shows that there has been some relaxation due to the creep of the rock salt. On the test surface, after 129 days the maximum principal stress peaks at 1.3 MPa.
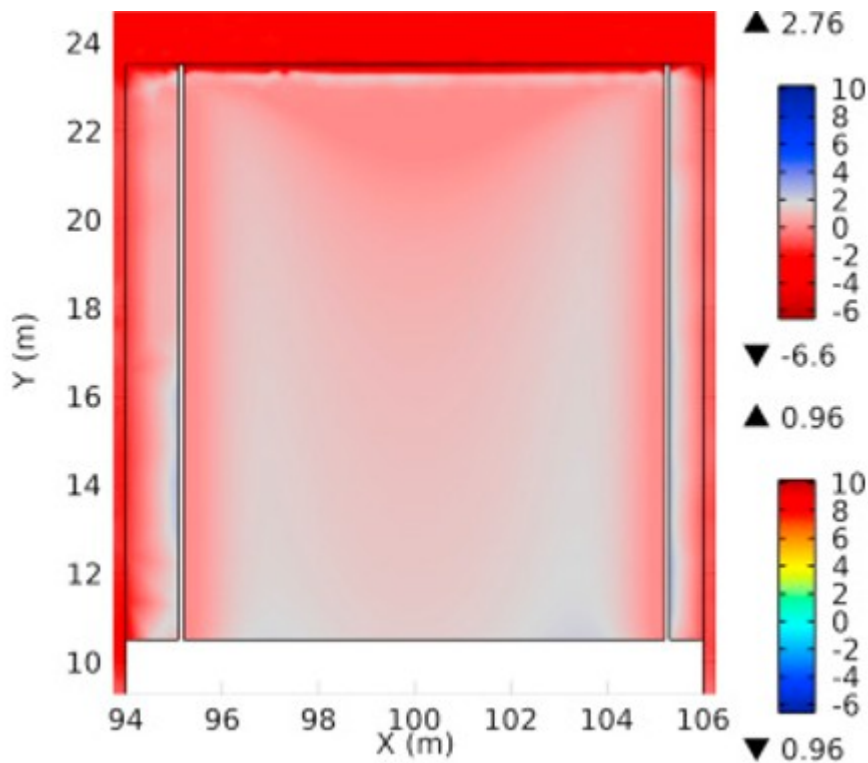

Fig. 8. Maximum principal stress (MPa) at the surface of the salt block after excavation ($t=0$). The principal stresses at locations P1-P5 (see Fig. 3) are displayed (bottom color table). The same scale is used in Fig. 8, Fig. 9, Fig. 10, Fig. 11, Fig. 12.
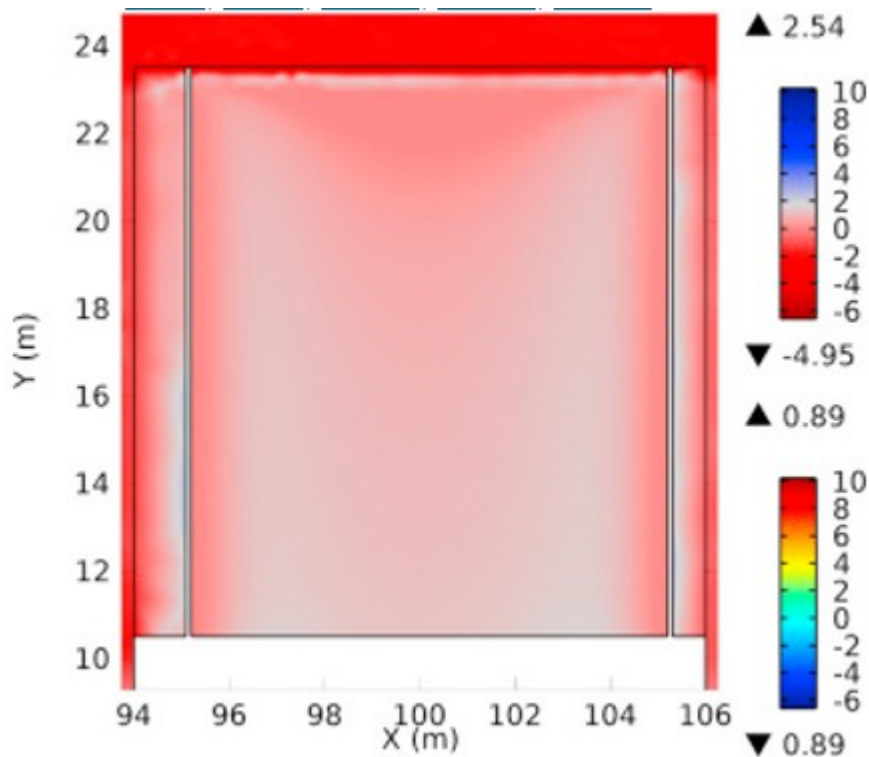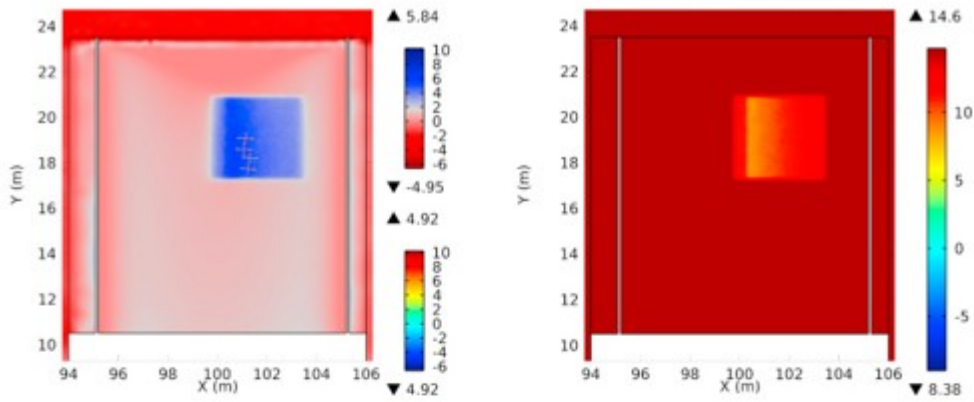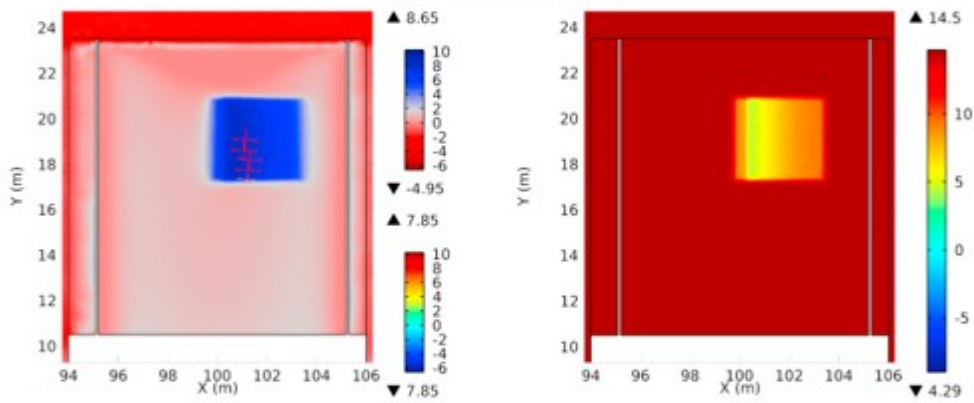
Fig. 9. Maximum principal stress (MPa) at the surface of the salt block before the beginning of the first cycle (*t*=129 d).
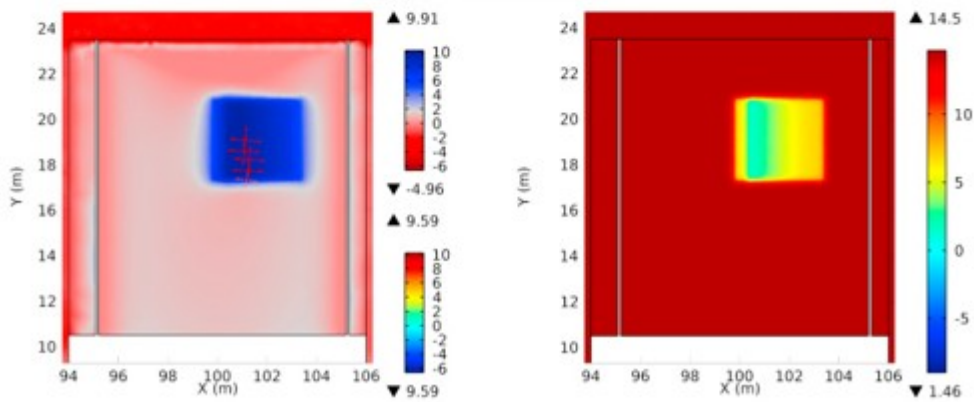
Fig. 10, Fig. 11 show the maximum principal stress and the temperature at different moments of the first cooling stage. Note that the temperature profile at *t*=129+28 d (cooler temperatures close to the rear door of the chamber) is due to the fact that the fans in the front area stopped working at *t*=129+12 d, and were not repaired until the first warming period. From the plots shown, it can be seen that as temperature decreases the stress state becomes more tensile and exceeds the tensile strength of the rock salt. Since these modeling results have been obtained with a continuum approach they are less accurate after the onset of fracturing; nevertheless, the computed stresses suggest that the emplacement and orientation of fracture initialization are fairly well reproduced numerically. Indeed, the first fracture was observed during the experiment at location P3 in Fig. 3, and the computed results displayed in Fig. 10, Fig. 11 show maximum stress values in this zone. Likewise, the orientation of the main fracture in Fig. 3is consistent with the orientation of the least compressive stress shown in these figures.

Fig. 10. Numerical results at the surface of the salt block during the first cooling stage. Left: maximum principal stress (MPa). Right: temperature (°C).

(a) $t=129$ d+6 h

(b) $t=129$ d+12 h

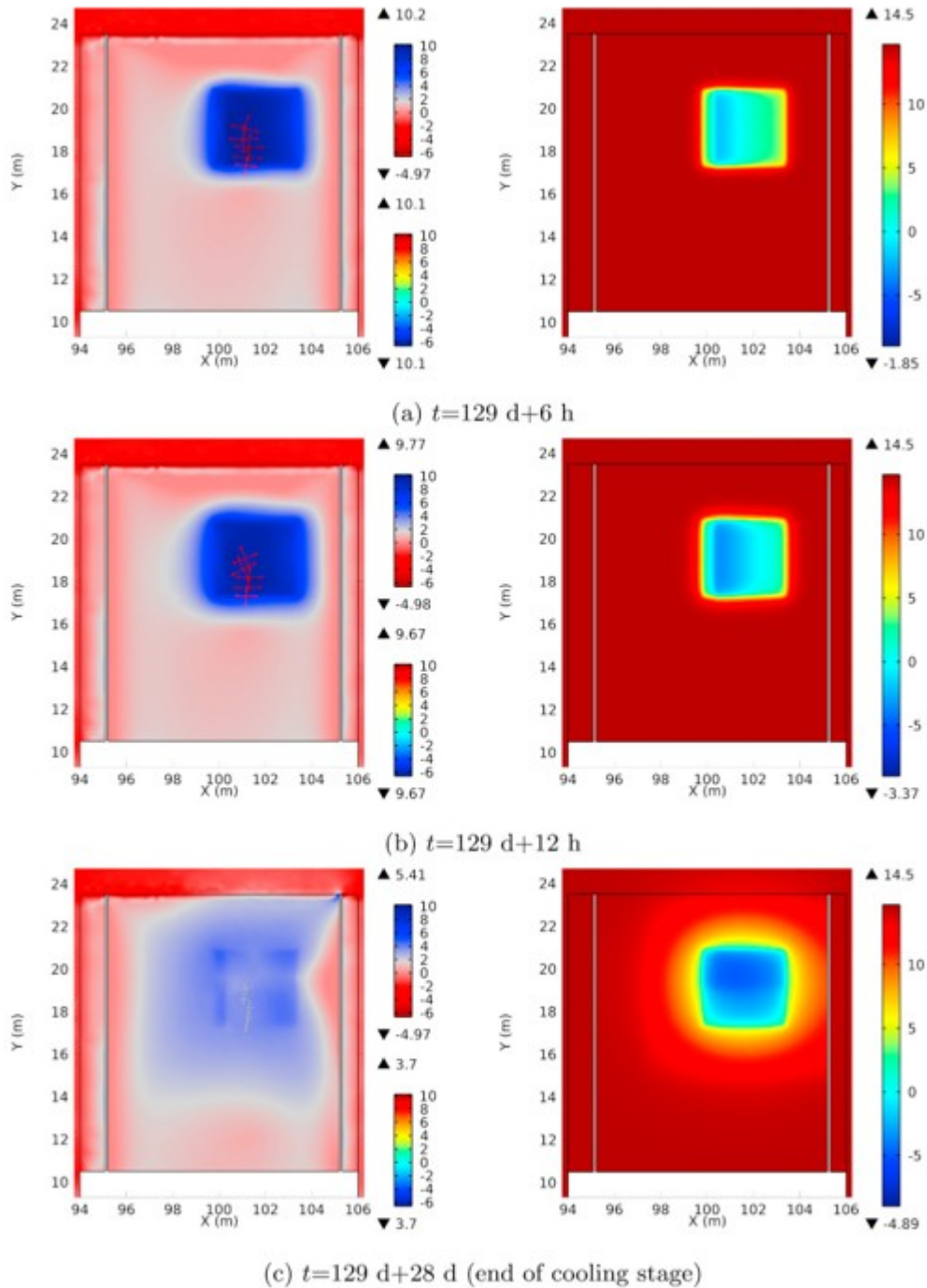(c) $t=129$ d+28 d (end of cooling stage)

Fig. 11. Numerical results at the surface of the salt block during the first cooling stage. Left: maximum principal stress (MPa). Right: temperature (°C).

We highlight that the main factor affecting the thermal stress is the linear thermal expansion coefficient (Eq. (2)). Indeed, given the short time in which fractures develop, time-dependent processes play a secondary role in this case. As Fig. 10 shows, after 30 minutes of cooling the temperature in the area where the first fracture was observed is about 9 °C, and the least

compressive stress is about 8 MPa; this value is consistent with the stress change estimated using $-\alpha_{th}E\Delta T/(1-2\nu)$.

The results at the end of the first cycle are shown in Fig. 12. As it can be seen, the temperature has come back to the initial value (14.5 °C), but a slight difference is observed in the stresses, due to the non-elastic response of the rock salt.
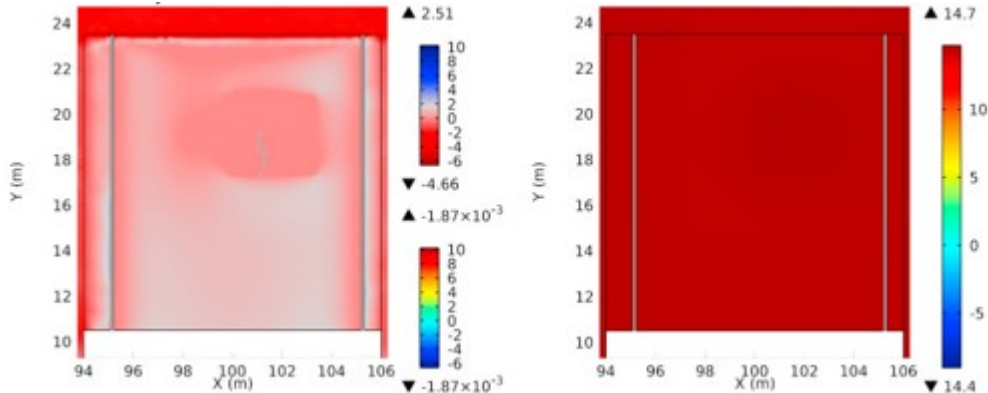

Fig. 12. Numerical results at the surface of the salt block at the end of the first cycle (t=129+62=191 d). Left: maximum principal stress (MPa). Right: temperature (°C).

Fig. 13 displays the maximum principal stress at three locations during the first 12 hours of cooling: P3 (surface of block), a point 50 cm below P3and a point 1 m below P3. The air temperature inside the chamber is also plotted. Note that below the salt surface, the maximum principal stress decreases initially due to the stress redistribution imposed by the compatibility requirement. Assuming that the tensile strength of the rock salt is 1.5 MPa, these numerical results suggest that the tensile strength at location P3 was reached after about 8 minutes of cooling, and after about 10 hours 50 cm below P3. During the experiment, the first fracture was visible at P3 after about 6 hours, which suggests its creation started at an earlier time. Taking into account the sensitivity of the results to parameters such as the thermal expansion coefficient of the rock salt or the Young's modulus of the underlying marl layer, the predicted timing of fracture creation can be considered satisfactory.
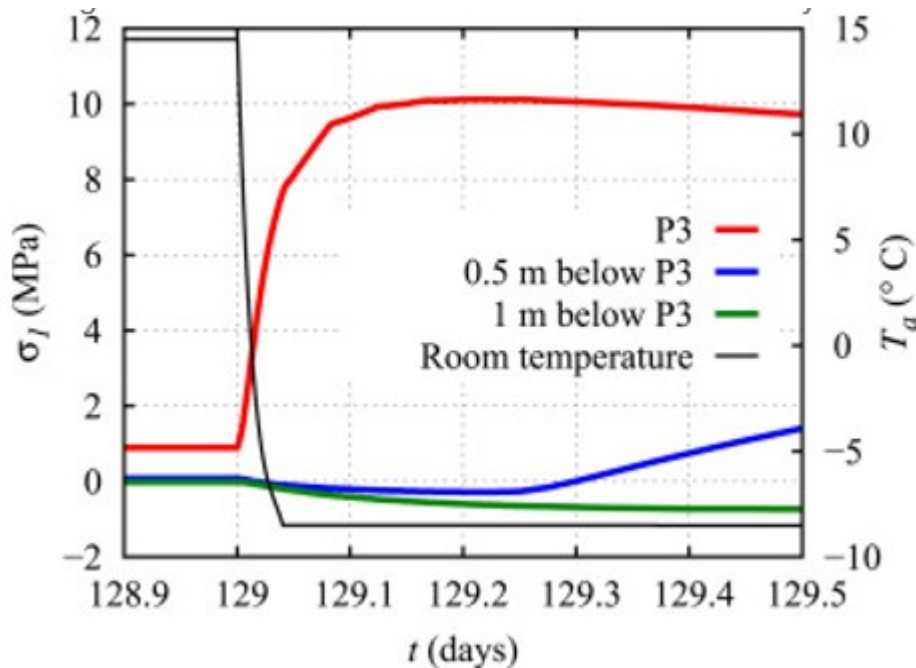
Fig. 13. Evolution of the maximum principal stress during the first 12 h of cooling at three locations.

Finally, Fig. 14 displays the maximum principal stress on a vertical plane across the chamber (plane x=101.17 m, which intersects the fracture visible during the first cycle), at the times displayed in Fig. 9, Fig. 10, Fig. 11, Fig. 12. Although during the first hours large tensile stressesconcentrate in the upper part of the block (first 80 cm), at the end of the first cooling phase large tensile stresses are predicted deeper than 1 m from the top of the salt block (due to propagation of cooling), which is in agreement with the observed depth of penetration of the main fracture, see Fig. 4. Overall, from Fig. 8, Fig. 9, Fig. 10, Fig. 11, Fig. 12, Fig. 13, Fig. 14, it can be concluded that the modeling results reproduce the location, orientation, timing and depth of penetration of the first fracture quite satisfactorily.
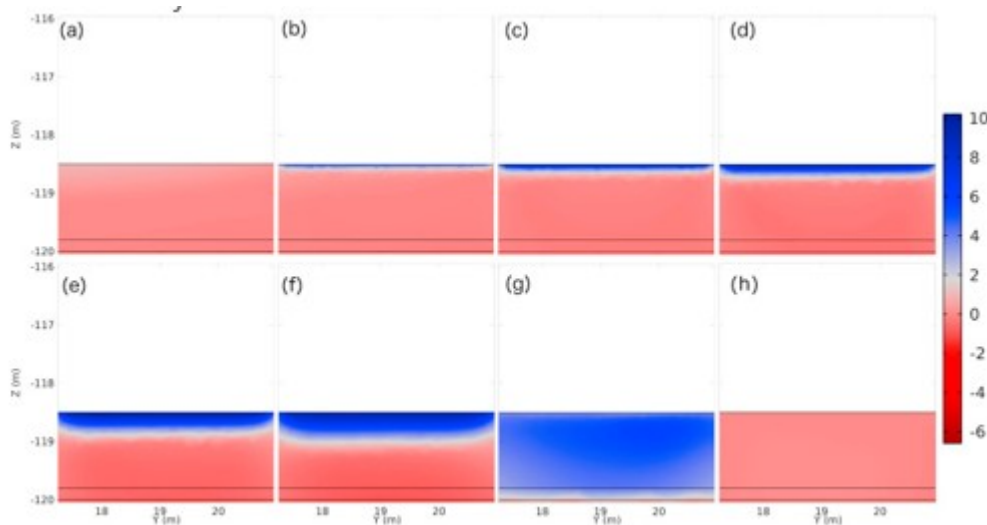
Fig. 14. Maximum principal stress (MPa) on a vertical plane across the chamber (plane x=101.17 m, between y=17.3 m and y=20.9 m), in the area where fractures were first observed. (a) t=129 d; (b) t=129 d+30 min; (c) t=129 d+40 min; (d) t=129 d+2 h; (e) t=129 d+6 h; (f) t=129 d+12 h; (g) t=129 d+28 d; (h) t=129 d+62 d.

4. Discussion

The test was conducted under particular conditions that did not aim at reproducing a salt storage cavern, but rather, at verifying whether a rapid temperature drop could lead to fracturing. In this context, the test specifications required that fracturing be favored as much as possible. To comply with these specifications, the initial stress state in the salt block was minimized by additionally cutting the two slots. This way, any thermally-induced tensile stress would only be balanced by the very low in situ stresses, thereby facilitating fracturing (i.e., this is a conservative scenario). Moreover, the applied cooling rate was high enough to favor the onset of fractures. Indeed, as the cooling rate increases heat transfer with the surrounding rock is much more limited, and large temperature changes concentrate close to the cooled surface, thereby favoring the creation of fractures.

Similarly, the test specifications required that temperature changes extend well beyond the test surface. To meet this requirement, cooling was maintained for 28 days during each cycle, whereas in a salt cavern under high frequency cycling, the withdrawal phase is much shorter. This leads to a conservative scenario as well.

The test demonstrated that tensile fracturing induced by rapid cooling is possible. However, despite the rather extreme scenario tested (very low initial stresses, aggressive cooling rate, long cooling periods), the depth of penetration of the fractures remained limited (<2m) through the cooling stages, which, given the size of a storage cavern, suggests that the effects of thermally-induced fractures are quite restricted (areas likely to be more sensitive are around the well or those with irregular shapes). Nevertheless, to stay on the safe side the existing design criteria and operational conditions should be adapted to minimize the effects of rapid depressurizations.

Finally, during this test, the rock salt was subjected to low (and negative) temperatures—a domain that is rarely investigated, but that is important in the context of high frequency cycling. In the modeling presented, temperature effects are extrapolated from the domain usually studied in laboratory tests (T> 20 °C). There is currently no sound evidence that the viscoplastic behaviour of rock salt is the same for high and low (even negative) temperatures, particularly since the viscous strain-ratedecreases non-linearly as temperature decreases. Research should be conducted on this matter to gain more insight.

5. Conclusions

To further investigate the impacts of high frequency cycling on the integrity of rock salt, a unique thermo-mechanical test was performed in the Varangéville salt mine (France). The experiment consisted in cooling rapidly several times a salt surface of 10 m^2 ($\Delta T=-20$ °C in about 8 h), and extensive monitoring was set up to track the thermo-mechanical response of the test surface and the underlying salt block, including possible fracture creation and propagation. The test was designed to favor fracturing, and as such, it does not reproduce a typical storage cavern. Many micro-fractures (imperceptible to the naked eye) and a few macro-fractures were created during the experiment, and their extension decreased with the number of cycles.

Thermo-mechanical modeling was performed after the test to help interpret experimental results and to evaluate the capabilities of the numerical tools commonly used in cavern design to reproduce the experimental observations. The location, orientation and timing of the first fracture were reproduced satisfactorily. This information is important at the design stage, since fractures should be avoided to ensure cavern integrity. The rather good agreement between experimental and modeling results suggest that thermo-mechanical modeling can assist in the study of the effects of rapid cooling on the integrity of rock salt, and therefore assist in the definition of a salt cavern storage project.

From the storage cavern perspective, the experiment demonstrated that tensile fracturing induced by rapid cooling is possible. In this sense, even if more research is needed, current design criteria and operational conditions should be adapted to minimize the effects of rapid depressurizations.

References

1

Bays C. Use of salt solution cavities for underground storage. In: Bersticker, Hoekstra, Hall, (Eds.), *Proceedings of the 1st World Salt Symposium*, Cleveland, OH; 1962: 564–578.

2

Thoms R, Gehle R. A brief history of salt cavern use. In: Geertman (Ed.), *Proceedings of the 8th World Salt Symposium*, The Hague; 2000: 207–214.

3

Hoather H, Challinor D. The use of salt cavities for the disposal of waste. In: *Proceedings of SMRI Fall Meeting*, Hannover; 1994.

4

Gillhaus A. Natural gas storage in salt caverns - present status, developments and future trends in Europe. In: *Proceedings of SMRI Fall Meeting*, Basel; 2007.

5

Wolters R, Lux K-H, Düsterloh U. Evaluation of rock salt barriers with respect to tightness: Influence of thermomechanical damage, fluid infiltration and sealing/healing. In: Bérest, Ghoreychi, Hadj-Hassen, Tijani, (Eds.), *Proceedings of Saltmech7*, Paris; 2012: 425–434.

6

O. Schulze, T. Popp, H. Kern**Development of damage and permeability in deforming rock salt**

Eng Geol, 61 (2–3) (2001), pp. 163-180, 10.1016/S0013-7952(01)00051-5

7

J. Stormont, J. Daemen**Laboratory study of gas permeability changes in rock salt during deformation**

Int J Rock Mech Min Sci Geomech Abstr, 29 (4) (1992), pp. 325-342, 10.1016/0148-9062(92)90510-7

8

C. Guo, L. Pan, K. Zhang, C.M. Oldenburg, C. Li, Y. Li**Comparison of compressed air energy storage process in aquifers and caverns based on the Huntorf CAES plant**

Appl Energy, 181 (2016), pp. 342-356, 10.1016/j.apenergy.2016.08.105

9

K. Staudtmeister, R. Rokahr**Rock mechanical design of storage caverns for natural gas in rock salt mass**

Int J Rock Mech Min Sci, 34 (3–4) (1997), 10.1016/S1365-1609(97)00199-8

[300.e1–300.e13]

10

Staudtmesiter K, Schmidt T. Comparison of different methods for the estimation of primary stresses in rock salt mass with respect to cavern design. In: Geertman (Ed.), *Proceedings of the 8th World Salt Symposium*, The Hague; 2000: 331–335.

11

K. Serbin, J. Ślizowski, K. Urbańczyk, S. Nagy**The influence of thermodynamic effects on gas storage cavern convergence**

Int J Rock Mech Min Sci, 79 (2015), pp. 166-171, 10.1016/j.ijrmms.2015.08.017

12

Sobolik S, Ehgartner B. Effect of cavern shapes on cavern and well integrity for the strategic petroleum reserve. In: Wallner, Lux, Minkley, Hardy-Jr, (Eds.), *Proceedings of Saltmech6*, Hannover; 2007: 353–361.

13

Minkley W, Knauth M, Fabig T, Farag N. Stability and integrity of salt caverns under consideration of hydro-mechanical loading. In: Roberts, Mellegard, Hansen, (Eds.), *Proceedings of Saltmech8*, Rapid City, SD; 2015: 217–227.

14

Costa A, Costa P, Amaral C, Poiate E. Jr., Computer modeling applied in the design of salt caverns for natural gas storage. In: Roberts, Mellegard, Hansen, (Eds.), *Proceedings Saltmech8*, Rapid City, SD; 2015: 265–271.

15

S. Heusermann, O. Rolfs, U. Schmidt**Nonlinear finite-element analysis of solution mined storage caverns in rock salt using the Lubby2 constitutive model**

Comput Struct, 81 (8–11) (2003), pp. 629-638, 10.1016/S0045-7949(02)00415-7

16

Khaledi K, Mahmoudi E, Datcheva M, Schanz T. Analysis of compressed air storage caverns in rock salt considering thermo-mechanical cyclic loading, Environ Earth Sci 75 (15). http://dx.doi.org/10.1007/s12665-016-5970-1.

17

Brouard B, Bérest P, Djizanne H, Frangi A. Mechanical stability of a salt cavern submitted to high-frequency cycles. In: Bérest, Ghoreychi, Hadj-Hassen, Tijani, (Eds.), *Proceedings of Saltmech7*, Paris; 2012: 381–389.

18

A. Ozarslan**Large-scale hydrogen energy storage in salt caverns**

Int J Hydrog Energy, 37 (19) (2012), pp. 14265-14277, 10.1016/j.ijhydene.2012.07.111

19

P. Bérest, B. Brouard, H. Djakeun-Djizanne, G. Hévin**Thermomechanical effects of a rapid depressurization in a gas cavern**

Acta Geotech, 9 (1) (2014), pp. 181-186, 10.1007/s11440-013-0233-8

20

P. Sicsic, P. Bérest**Thermal cracking following a blowout in a gas-storage cavern**

Int J Rock Mech Min Sci, 71 (2014), pp. 320-329, 10.1016/j.ijrmms.2014.07.014

21

Karimi-Jafari M, Gatelier N, Brouard B, Bérest P, Djizanne H. Multi-cycle storage in salt caverns. In: *Proceedings of SMRI Fall Meeting*, York; 2011.

22

Pellizzaro C, Bérest P, Brouard B, Karimi-Jafari M. Nouvelles problématiques poseés par le cyclage thermo-mécanique en cavités salines. In: *Proceedings Journées Nationales de Géotechnique et de Géologie de l'Ingénieur*, Nancy; 2012.

23

Djizanne H, Bérest P, Brouard B. Tensile effective stresses in hydrocarbon storage caverns. In: *Proceedings SMRI Fall Meeting*, Bremen; 2012.

24

Bérest P, Djizanne H, Brouard B, Hévin G. Rapid depressurizations: can they lead to irreversible damage ? In: *Proceedings SMRI Spring Meeting*, Regina; 2012.

25

Zapf D, Staudtmeister K, Rokahr R. Analysis of thermal induced fractures in rock salt. In: *Proceedings SMRI Spring Meeting*, Regina; 2012.

26

Hévin G, Charnavel Y, Balland C, et al. *Perform a Thermo-mechanical Test in a Salt Mine, as part of SMRI's Research Program on High Frequency Cycling of Salt Storage Caverns*, SMRI Research Report RR 2016-1; 2016.

27

Balland C, Billiotte J, Bigarré P, et al. Acoustic monitoring of a thermo-mechanical test simulating withdrawing in a gas storage salt cavern, Int J Rock Mech Mining Sci; 2017 [Submitted for publication].

28

N. Moës, J. Dolbow, T. Belytschko**A Finite element method for crack growth without remeshing**

Int J Numer Methods Eng, 46 (1) (1999), pp. 131-150

29

V. Vilarrasa, S. Olivella, J. Carrera, J. Rutqvist**Long term impacts of cold CO$_2$ injection on the caprock integrity**

Int J Greenh Gas Control, 24 (Supplement C) (2014), pp. 1-13, 10.1016/j.ijggc.2014.02.016

30

Tijani M, Vouille G, Hugout B. Le sel gemme en tant que liquide visqueux. In: *Proceedings of the 5th Congress of the International Society for Rock Mechanics*, Melbourne; 1983: 241–246.

31

COMSOL AB, *COMSOL Multiphysics Reference Manual, v4.4*; 2013.

32

S.-M. Tijani**Short description of VIPLEF code**

Dev Geotech Eng, 79 (1996), pp. 507-511, 10.1016/S0165-1250(96)80039-3

33

Tijani M. *Contribution à l'étude thermomécanique des cavités réalisées par lessivage dans des formations géologiques salines, Habilitation à diriger des recherches*. Université Pierre et Marie Curie; 2008.

34

Tijani M. *VIPLEF3D - Notice d'utilisation*, MINES ParisTech; 2016.